Full-Potential Analysis of a Supersonic Delta Wing/Body

O. J. Rose*
Planning Research Corporation, Hampton, Virginia
David S. Miller† and James L. Pittman‡
NASA Langley Research Center, Hampton, Virginia
and
P. R. Ashill§ and J. L. Fulker¶
Royal Aircraft Establishment, Bedford, England, United Kingdom

Experimental spanwise pressure distributions for a 60 deg delta wing/body of approximate fineness ratio 7.6 have been obtained and compared to predictions using full-potential theory. Analysis was performed at Mach 1.6 for angles of attack in the range of 0.8–10 deg, and for Mach numbers ranging from 1.4 to 1.8 at lift coefficient 0.3. The intent of the study was to examine an attached flow approach for maneuver wing design in the presence of a fuselage. For the Mach number and angle-of-attack conditions considered, the full-potential theory accurately modeled the pressure distributions, provided the flow remained attached. By combining the full-potential theory results with empirical shock-induced separation criteria, it was found that the onset of shock-induced separation can be predicted.

Nomenclature

c = local chord
c_o = wing centerline chord, used as reference length (Fig. 1)
C_L = lift coefficient
C_p = static pressure coefficient
M = freestream Mach number
M_c = crossflow Mach number
p = static pressure; coordinate direction in projection plane (Fig. 2)
q = coordinate direction in projection plane (Fig. 2)
r = radial coordinate in mapped plane (Fig. 2)
r_{LE} = leading-edge radius of airfoil section
R = distance of spherical cut from configuration apex (Fig. 2)
x = lateral Cartesian coordinate measured from configuration apex (Fig. 2)
y = vertical Cartesian coordinate measured from configuration apex (Fig. 2)
z = longitudinal Cartesian coordinate measured from configuration apex (Fig. 2)
$\bar{z}$ = longitudinal location measured from wing virtual apex (Fig. 1)
α = angle of attack
η = dimensionless spanwise location referenced to leading edge, x/x_{LE}
θ = angular coordinate in mapped plane (Fig. 2)

Subscripts
LE = leading edge
1,2 = conditions just upstream and downstream of crossflow shock, respectively

Introduction

THE next generation of combat aircraft will be required to achieve high sustained turn rates over a wide range of speeds.[1] This naturally leads to the need for improved methods of nonlinear aerodynamic design to reduce drag at maneuver lift coefficients. At these high lift coefficients, two different approaches are available for wing design: a separated flow approach and an attached flow approach. The separated-flow approach employs a sharp leading-edge wing to produce separation in the form of a controlled leading-edge vortex; the attached flow approach employs wing camber and rounded leading edges to reduce leading-edge pressure gradients and thereby promote attached flow. The attached flow approach is addressed in this paper.

For supersonic speeds at maneuvering conditions, the attached flow wing design problem is complicated by the nonlinear transonic character of the crossflow. At high lift coefficients, strong crossflow shock waves can develop on the upper surface, possibly leading to shock-induced flow separation and high drag. A reliable design methodology must, therefore, be based on a suitable understanding of the flow. In practice, any viable procedure will emerge as a blend of accurate predictive capability enhanced by empirical correlations. Previous research has shown that the nonlinear full-potential equation sufficiently represents the flow physics to be used as an accurate design/analysis method for attached flow conditions at low to moderate supersonic speeds. Previously, a code based on the conical full-potenial equation was developed[2] and applied to a conical wing problem.[3] This code was extended to the fully three-dimensional full-potential equation[4,5] and was used to design a maneuver wing[6] at Mach number 1.62 and $C_L = 0.4$. Subsequently, this three-dimensional method was used to analyze more complex fighter geometries.[7,8] Additional applications to other configurations and to supersonic airfoil optimization are presented in Refs. 9–13.

Presented as Paper 88-0480 at the AIAA 26th Aerospace Sciences Meeting, Reno, NV, Jan. 11–14, 1988; received Feb. 5, 1988; revision received Sept. 1, 1988.

*Supervisor, Aeronautical Sciences Unit, Aerospace Technologies Division. Member AIAA.
†Head, Supersonic/Hypersonic Aerodynamics Branch, High-Speed Aerodynamics Division. Associate Fellow AIAA.
‡Aero-Space Technologist, Supersonic/Hypersonic Aerodynamics Branch, High-Speed Aerodynamics Division. Associate Fellow AIAA.
§Principle Scientific Officer.
¶Senior Scientific Officer.

Model Description and Test Conditions

The layout of the half-span model is illustrated in Fig. 1. The fuselage is essentially of rectangular cross section with rounded corners. The wing has a modified 60 deg sweep delta planform having 4% maximum thickness ratio airfoil sections and is mounted low on the fuselage. A large leading-edge radius of approximately $r_{LE} = 0.003c$, which reduces leading-edge expansion gradients, is used to promote attached flow at maneuver levels of lift. The wing has a camber and twist distribution based on that of an earlier linearized-theory cruise-lift design.[14] The wing in this study was developed by using a Prandtl-Glauert scaling law to scale the mean camber ordinate of an earlier wing, which was designed for $M = 2.2$ and $C_L = 0.05$, to one having design conditions of $M = 1.5$ and $C_L = 0.8$.

As indicated in Fig. 1, wing-surface pressures were measured at nine streamwise stations corresponding to $\bar{z}/c_o$ locations of 0.28, 0.37, 0.45, 0.54, 0.62, 0.71, 0.79, 0.87, and 0.96. The body was also instrumented with pressure orifices on the side along the centerline.

The tests were performed in the 8 × 8-ft wind tunnel at the Royal Aircraft Establishment Bedford facility at a unit Reynolds number of 4×10^6/ft and Mach numbers of 1.4, 1.6, and 1.8. Boundary-layer transition was ensured on both surfaces of the wing and on the nose of the body through the use of strips of glass beads.

Nonlinear Full-Potential Aerodynamic Method

The NCOREL code solves the nonconservative form of the steady-flow, three-dimensional, full-potential equation written in spherical coordinates. Exact tangent-flow boundary conditions are specified on the body surface. The three-dimensional full-potential equation written in a spherical coordinate system reduces identically to the conical (two-dimensional) full-potential equation in the initial data plane. The conical equation is used to initiate the three-dimensional marching solution, which then marches implicitly in space along concentric spheres at user-specified radii. Implicit marching was chosen because this method allows a larger step size than is possible with explicit marchers.

At a given marching station, the spherical cut is mapped into a planar, rectangular computational mesh by a series of conformal mappings, as shown in Fig. 2. The mapped full-potential equation is approximated in the computational space by a finite-difference analog. The resulting set of linear simultaneous equations is solved using a successive line over relaxation technique.

Grid generation is controlled by specifying marching step size and the number of grid points for each spherical solution plane. The grid points in each spherical solution plane are evenly spaced in the radial direction between the inner boundary (the geometry) and the outer boundary (the bow shock). The grid points around the geometry are clustered by a cosine function at the leading edge, since this is known to be a region of large flow gradients. The other aspects of grid generation and mapping are internal to the code.

An extensive treatment of the mathematical and numerical formulation of the NCOREL code is given in Refs. 4 and 5. A careful discussion of the method together with applications to missile bodies is presented in Ref. 13.

Geometry Modeling

Figure 3 shows a drawing of a pointwise representation of the model. Inspection of Fig. 3 reveals two noteworthy features of the geometry which caused some practical difficulties in applying the NCOREL full-potential method. First, the vertical fuselage side where the wing is attached to the body presents a severe practical test of the conformal mapping method used in NCOREL. Second, the sharp corner at the wing-body intersection is not mapped precisely at each cross section and also produces a degrading effect on the stability of the computations due to the discontinuous slope at the corner.

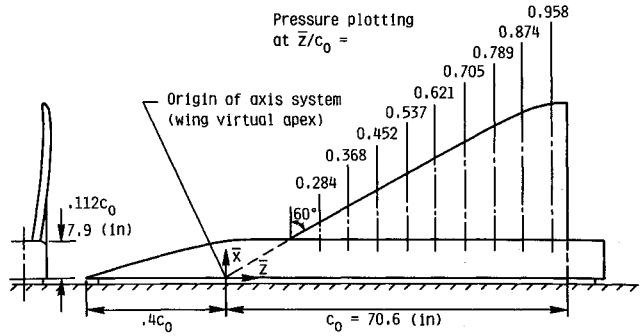

Fig. 1 General layout of model showing pressure orifice locations.

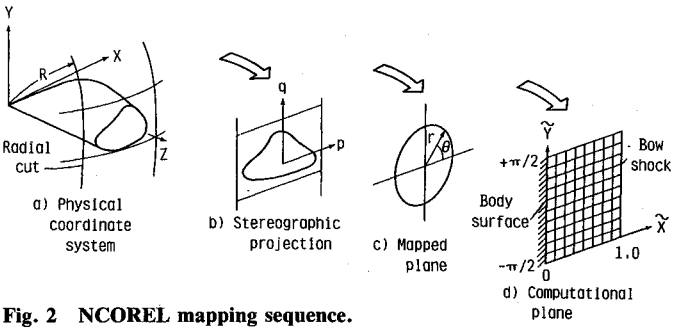

Fig. 2 NCOREL mapping sequence.

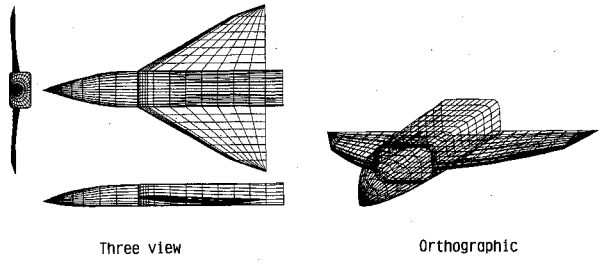

Fig. 3 Wing/fuselage representation for full-potential calculation.

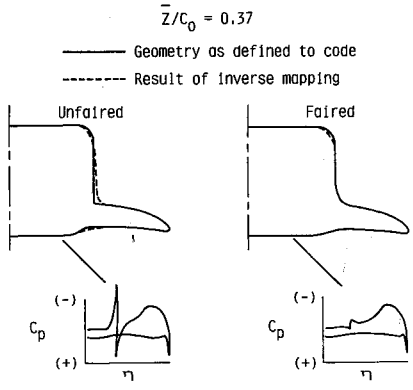

Fig. 4 Result of mapping and geometry modification.

These two features can be further appreciated by examination of Fig. 4, which shows a cross section of the configuration at station $\bar{z}/c_o = 0.37$. The solid line in Fig. 4a shows the wing/body as it is input to the code where the vertical side is clearly evident. The dashed line in Fig. 4a shows the result of the conformal and inverse mapping, which ideally should recover the input cross section. The loss of fidelity in the region of the vertical side is clearly evident. The loss of geometric resolution on the body side is due to the method of clustering surface

points in the NCOREL code. The Cartesian definition of the body surface in each crossflow plane is mapped into a near circle, which is then used to define the grid points in polar coordinates. The body surface grid points are clustered at the leading edge of the wing by a cosine function. This yields high geometric resolution near the wing leading edge; however, the geometric resolution is reduced as the centerline is approached. From a flow solution standpoint, the presence of the near-vertical side and sharp corner at the wing/fuselage intersection caused numerical oscillations which became amplified and eventually diverged as the solution marched aft. To overcome this obstacle, a slight fairing was introduced in the wing/fuselage juncture region to relieve the abrupt geometry gradient. The extent of this fairing, input geometry before mapping (solid line) and after inverse mapping (dashed line), is shown in Fig. 4b. Here it is seen that the dashed and solid lines are virtually identical except for a slight difference in the vicinity of the fuselage shoulder.

Comparison of Full-Potential Predictions with Experimental Results

Effect of Marching Step Size and Crossflow-Plane Grid Density on Solution Accuracy

Figure 5 shows the effect of changes in marching step size on the computed pressure distributions. The cases shown are for $M = 1.6$, $\alpha = 3.3$ deg at stations $\bar{z}/c_o = 0.37$ and 0.54 and for a fixed crossflow-plane grid of 57×37. The 57 points are distributed around the half-plane and clustered near the leading edge by a cosine function, and the 37 points are evenly spaced between the body and the bow shock. Marching step size has very little effect on the windward or lower-surface pressure predictions. The lower-surface pressure predictions for all three marching step sizes agree well with the experimental data. On the upper surface, for a step size of $0.04c_o$, the suction peak is grossly overpredicted, the error decreasing with increasing streamwise location. Halving the step size produces an accurate calculation of surface pressure, except for a slight overprediction of the leading-edge expansion at $\bar{z}/c_o = 0.37$ (Figs. 5a and 5c). Reducing the step size to $0.01c_o$ virtually eliminates the suction peak overprediction on the entire wing, as can be seen in Figs. 5b and 5d. It is seen from Fig. 5 that decreasing the marching step size does not resolve the pressure in the vicinity of the fuselage/wing intersection.

The effect of varying crossflow-plane grid density is given in Fig. 6. Shown are results for $M = 1.6$, $\alpha = 3.3$ deg at stations $\bar{z}/c_o = 0.37$ and 0.54 with grid densities of 57×37 and 29×19 at a fixed marching step size of $0.01c_o$. As was the case with the effect of varying marching step size, the effect of grid density variation is confined to the upper surface. The larger marching step size tended to predict a more negative expansion; by contrast, a more coarse crossflow-plane grid density tends to predict a less negative expansion. Furthermore, the effect of marching step size variation tended to decrease with increasing streamwise location, whereas he effect of crossflow-plane grid density variation is relatively insensitive to streamwise location for this particular marching step size. As was the case with marching step size, increasing crossflow-plane grid density does not resolve the pressure near the fuselage/wing interaction.

Previous experience with wings and blended wing/body combinations had indicated that a marching step size of 2–3% of the total configuration length and a crossflow-plane grid density of approximately 30×20 was an acceptable choice. The results given here indicate that a crossflow-plane grid density of approximately 60×40 together with a marching step size of about $0.01c_o$ ($\approx 0.7\%$ of configuration length) is an effective

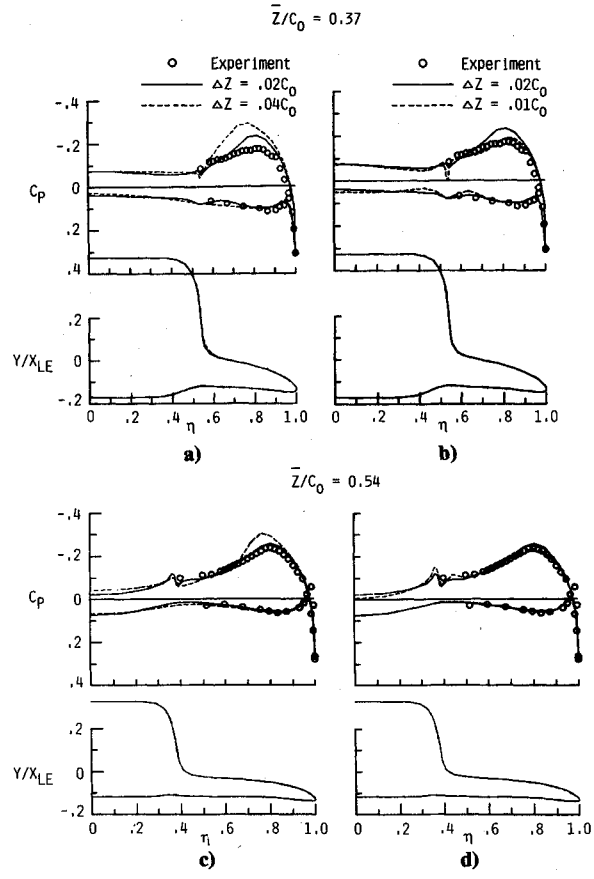

Fig. 5 Effect of varying step size in the marching direction ($M = 1.6$, $\alpha = 3.3$ deg, 57×37 grid).

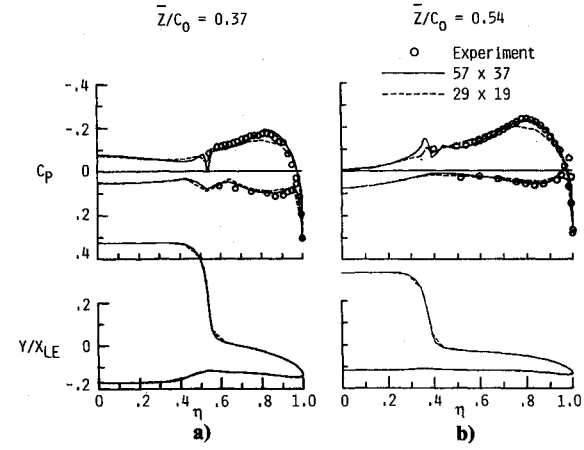

Fig. 6 Effect of varying grid density in the crossflow plane ($M = 1.6$, $\alpha = 3.3$ deg, $\Delta z = 0.01c_0$).

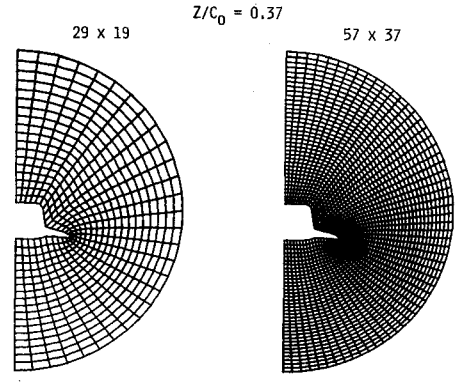

Fig. 7 Effect of varying grid density in the crossflow plane ($M = 1.6$, $\alpha = 3.3$ deg, $\bar{z}/c_0 = 0.37$).

choice for this particular configuration, which has a relatively low fineness ratio body. A crossflow grid density of 57 × 37 and step size of 1% root chord was used for all computations presented in the reminder of this paper. Shown in Fig. 7 is a comparison of the crossflow-plane grids at the indicated conditions and streamwise station. The body forms the inner boundary, and the bow shock the outer boundary. It is seen that the grid is clustered near the wing leading edge, where flow gradients are expected to be large.

Effect of Variation in Angle of Attack and Streamwise Location

Figures 8–11 show spanwise pressure distributions for $M = 1.6$, angles of attack $\alpha = 0.8$, 5.3, 7.8, and 10.3 deg, and streamwise stations corresponding to $\bar{z}/c_o = 0.37$ locations of 0.37, 0.54, and 0.71. For all stations at $\alpha = 0.8$ deg (Fig. 8), the crossflow stagnation point is located on the upper surface near the wing leading edge, as evidenced by the maximum C_p value in the experimental surface-pressure data and the NCOREL predictions. In general, all the pressure distributions can be characterized by a sharp suction peak on the lower wing surface near the leading edge and a more extensive region of suction pressure on the upper surface. The expansions around the leading edge are recompressed isentropically on the upper surface and remain attached. The isentropic and attached character of the recompression is evidenced by the smooth nature of the pressure distribution and by the NCOREL calculations, which indicate that the crossflow is subcritical. For this angle of attack, with attached flow on both the upper and lower surfaces, NCOREL correctly predicts the location of the cross-flow stagnation point at the leading edge and the sharp suction peak on the lower surface as well as the smooth pressure distribution on the upper surface. The anomalous spike on the upper surface near the fuselage/wing intersection was previously discussed.

For $\alpha = 5.3$ deg (Fig. 9), it is seen that the lower surface suction peak is absent. At station $\bar{z}/c_o = 0.37$, NCOREL calculations indicate that the crossflow remains subcritical, and the smooth nature of the pressure distribution further indicates that the flow recompresses isentropically on the upper surface at this station. Predictions of supercritical crossflow on the upper surface are obtained from NCOREL at stations $\bar{z}/c_o =$ 0.54 and 0.71, but the smoothness of the pressure

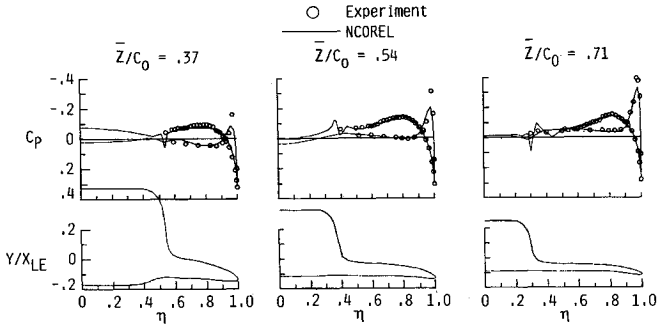

Fig. 8 Effect of variation in angle of attack and streamwise location ($M = 1.6$, $\alpha = 0.8$ deg).

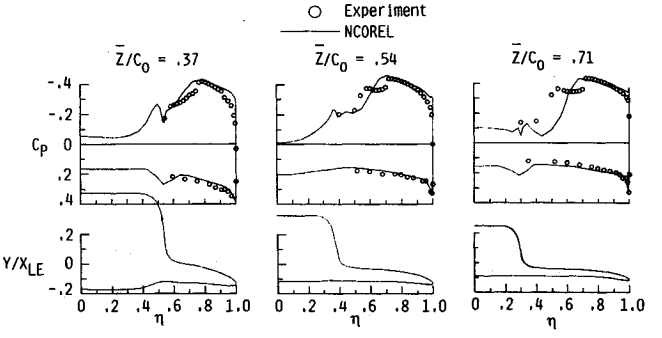

Fig. 11 Effect of variation in angle of attack and streamwise location ($M = 1.6$, $\alpha = 10.3$ deg).

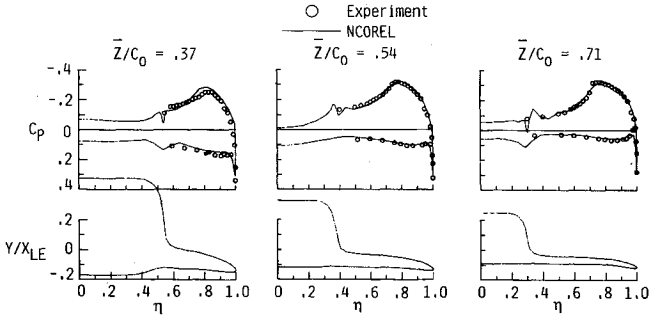

Fig. 9 Effect of variation in angle of attack and streamwise location ($M = 1.6$, $\alpha = 5.3$ deg).

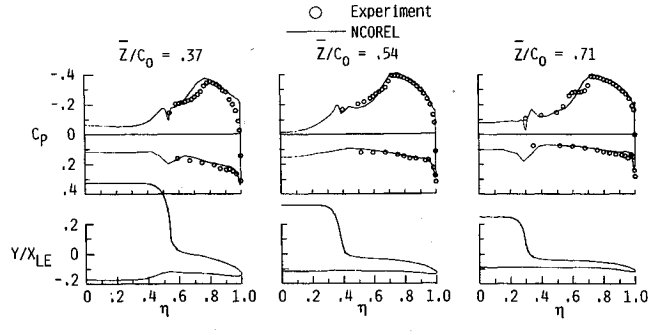

Fig. 10 Effect of variation in angle of attack and streamwise location ($M = 1.6$, $\alpha = 7.8$ deg).

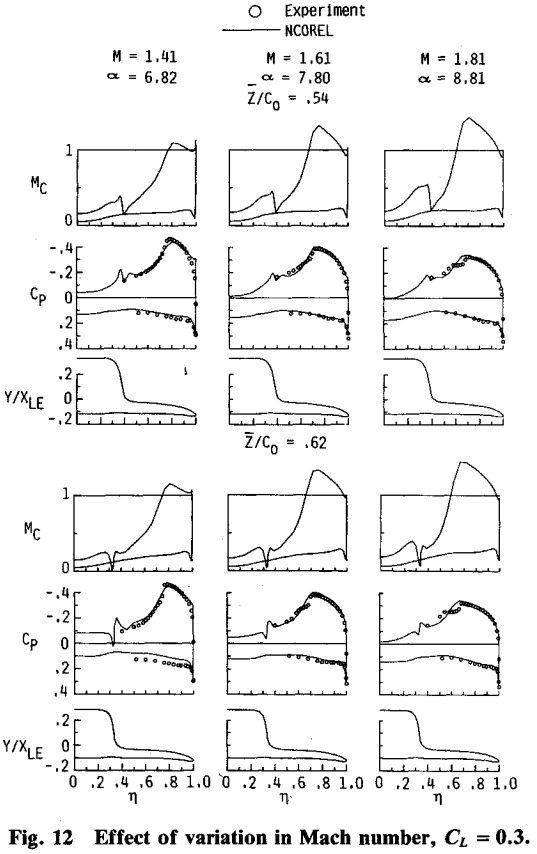

Fig. 12 Effect of variation in Mach number, $C_L = 0.3$.

distribution at $\bar{z}/c_o = 0.54$ does not have the steepness associated with a crossflow shock. By contrast, the predicted pressure $\bar{z}/c_o = 0.71$ suggests a smeared shock where the upper surface recompresses. In the experimental data, the pressure distributions on the upper surface are quite smooth at stations $\bar{z}/c_o = 0.37$ and 0.54, indicating isentropic recompression. At station $\bar{z}/c_o = 0.71$, a crossflow shock just inboard of the upper-surface expansion peak is clearly evident in the experimental data. Inboard of the crossflow shock, the excellent agreement between experiment and full-potential calculations indicates that it remains attached. Thus, for $\alpha = 5.3$ deg, the flow appears to be attached on both upper and lower surfaces, with good agreement between the NCOREL predictions and the experimental pressures. Flow visualization indicated that at stations downstream of $\bar{z}/c_o = 0.71$, the boundary layer thickened at the foot of the shock, suggesting incipient separation at these conditions.

For angle of attack $\alpha = 7.8$ deg (Fig. 10), the NCOREL predictions agree well with the experimental pressures on the lower surface at all streamwise stations. On the upper surface, the flow expands around the leading edge and recompresses through a crossflow shock just inboard of the upper-surface expansion peak. At stations $\bar{z}/c_o = 0.37$ and 0.54, the flow recompresses isentropically inboard of the shock, similar to the results at $\alpha = 5.3$ deg. For station $\bar{z}/c_o = 0.71$, the experimental pressures exhibit a pressure plateau just inboard of the crossflow shock, with a second abrupt recompression inboard of the plateau. This feature in the pressure distribution is not predicted by the full-potential method.

For $\alpha = 10.3$ deg (Fig. 11), the experimental pressure distributions on the upper surface exhibit the same characteristic of a crossflow shock, with a pressure plateau inboard of the shock followed by a second abrupt recompression for all streamwise stations, except at $\bar{z}/c_o = 0.37$. Flow visualization data taken during the wind-tunnel test indicated the presence of shock-induced separation at the conditions where the pressure plateau was present inboard of the crossflow shock. This interpretation is also supported by the results published in Refs. 3 and 6. Based on this evidence, shock-induced separation is assumed for pressure distributions of this type. Further discussion of shock-induced separation is given subsequently.

At $\alpha = 7.8$ and 10.3 deg (Figs. 10 and 11), where the smooth experimental pressure distribution inboard of the upper surface recompression indicates the presence of attached flow, the full-potential predictions are generally in good agreement with the measurements. Where the experimental pressure plateau inboard of the upper surface recompression indicates shock-induced separation, the full-potential calculations do not agree well with experiment, since full-potential theory does not admit separated flow.

Effect of Mach Number Variation

Figure 12 presents a comparison of the experimental and computed surface-pressure distributions and the computed surface crossflow Mach number distributions for a freestream Mach number variation of 1.4, 1.6, and 1.8 at a C_L of approximately 0.3. This information is given at $\bar{z}/c_o = 0.54$ and 0.62. At all three freestream Mach numbers, the computed crossflow Mach number is supercritical on an outboard portion of the upper surface. This region of supercritical flow becomes larger with increased freestream Mach number, the peak crossflow Mach number increases, and the drop of crossflow Mach number across the crossflow shock increases. A comparison of the computed and experimental surface-pressure distributions indicates that the full-potential method correctly predicts the expansion of the flow around the wing leading edge and onto the upper surface. Furthermore, the location and stength of the crossflow shock is correctly computed except for $M = 1.8$. For this Mach number and angle-of-attack combination, shock-induced separation is indicated by the experimental plateau at the foot of the crossflow shock. The lower-surface

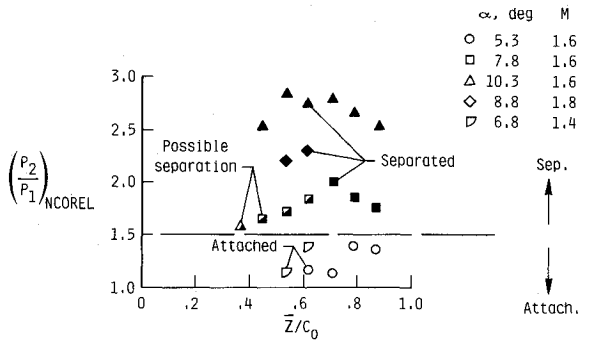

Fig. 13 Pressure correlation for predicting shock-induced separation.

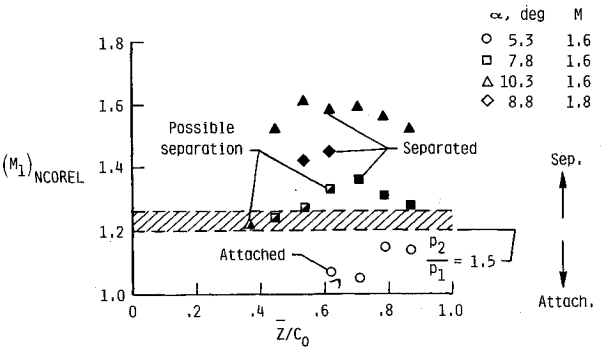

Fig. 14. Normal Mach number correlation for predicting shock-induced separation.

pressures are well predicted, except for $M = 1.4$ at $\bar{z}/c_o = 0.62$. The reason for this error in the full-potential calculation is not known.

Prediction of Shock-Induced Separation

Although full-potential theory does not model separated flow, full-potential calculations can be used together with an empirical criterion to indicate the possibility of shock-induced separation. A suitable empirical criterion for shock-induced separation of a turbulent boundary layer based on a threshold static pressure rise of $p_2/p_1 = 1.5$ through the crossflow shock is given in Ref. 15.

An independently determined but consistent criterion using a Mach number component normal to the shock is given in Ref. 16. For all the cases having a crossflow shock, the NCOREL computed values of p_2/p_1 and the experimentally determined flow types were correlated and compared to the $p_2/p_1 = 1.5$ criterion. The results are shown in Fig. 13. In the figure, filled symbols indicate shock-induced separated flow, open symbols indicate attached flow, and half-open symbols indicate cases of possible shock-induced separation. It is seen that every case of separated or possibly separated flow is located above the $p_2/p_1 = 1.5$ line, while every case of attached flow is located below the same line.

The predicted p_2/p_1 values were also expressed in terms of M_1, the local normal Mach number just upsteam of the crossflow shock. The results were classified similarly to the p_2/p_1 values and compared to the empirical observations given in Ref. 16. The comparison is shown in Fig. 14. The observations of Ref. 1 were for airfoils observed with both free and fixed transition. The normal Mach number at separation was in the range of $M_1 = 1.2$–1.26; this is shown by the cross-hatched band in Fig. 14. It is also noted that the $p_2/p_1 = 1.5$ criterion corresponds approximately to $M_1 = 1.2$, as calculated from one-dimensional gas dynamic relationships. It is clear that these results support and are consistent with a separation criterion based on $p_2/p_1 = 1.5$.

Considering the effect of changes in angle of attack on shock-induced separation at a fixed Mach number and streamwise station, the results of Figs. 13 and 14 indicate that the flow is first attached at the lower α and then becomes separated as α increases, as one would expect. To assess the effect of Mach number variation of shock-induced separation, it is noted that there is Mach number variation from $M = 1.4$ to 1.8 at stations $\bar{z}/c_o = 0.54$ and 0.62 for approximately fixed lift coefficient. As shown in Fig. 13, for $M = 1.4$ the flow is attached, for $M = 1.6$ possible shock-induced separation is indicated, and for $M = 1.8$ there is definite shock-induced separation.

Overall, the interpretation of the pressure plateau inboard of a crossflow shock, followed by another compression inboard of the plateau as shock-induced separation, is consistent with the empirical criterion of Ref. 15. Also, the correlations presented in Figs. 13 and 14 show that either of these separation criteria could be used together with full-potential computations as an effective wing design tool to prevent or to detect the occurrence of shock-induced separation.

Summary and Conclusions

Experimental spanwise pressure distributions for a wing/body configuration together with an NCOREL full-potential analysis have been presented. Results were given for Mach numbers of 1.4, 1.6, and 1.8 and for lift conditions ranging from cruise to maneuver. The leading-edge radius of the wing was large so that the flow would remain attached around the leading edge for maneuver lift conditions. In all cases where the experimental pressure distributions indicated the presence of attached flow, the full-potential predictions were in generally good agreement with the measurements. Discrepancies occurred in two situations. First, at all stations and conditions, there was a small anomalous pressure spike predicted on the upper surface in the vicinity of the wing/body junction. This was due to the abrupt change in geometry represented by the sharp corner. Second, there was disagreement at the higher lift coefficients in the regions where there was experimental evidence of shock-induced separation. This disagreement was expected, since the full-potential theory does not admit separated flow. Even at the higher lift coefficients, in those regions of attached flow, the full-potential results were in good agreement with the experiment.

The effect of crossflow plane grid density and marching step size was examined. Previous experience had indicated that a marching step size of 2–3% of total configuration length and a crossflow grid density of aproximately 30×20 was a suitable choice. The results presented here indicate that a marching step size of approximately 1% of configuration length and a crossflow plane grid density of approximately 60×40 grid points is an improved guideline for wing/body configurations of low fineness ratio.

Evidence of shock-induced separation was examined in light of an empirical separation criterion based on a predicted static pressure rise of 50% through the crossflow shock. A static pressure rise of this magnitude corresponds to a Mach number normal to the shock of approximately 1.2. It was found that the full-potential predictions could consistently be used to indicate the possibility of shock-induced separation based on this empirical criterion.

For designing wings for maneuver, if the design approach is based on attached flow and appropriate empirical methods are employed to indicate possible shock-induced separation, the full-potential method is capable of being used as an effective design tool.

References

[1]Hirst, M., "The Next Generation Fighters," *International Defense Review,* Vol. 17, No. 8, 1984.

[2]Mason, W. H. and Rosen, B. S., "The COREL and W12SC3 Computer Programs for Supersonic Wing Design and Analysis," NASA CR-3676, Dec. 1983.

[3]Miller, D. S., Landrum, E. J., Townsend, J. L., and Mason, W. H., "Pressure and Force Data for a Flat Wing and a Warped Conical Wing Having a Shockless Recompression at Mach 1.62," NASA TP-1759, April 1981.

[4]Siclari, M. J., "The NCOREL Computer Program for 3-D Nonlinear Supersonic Potential Flow Computations," NASA CR-3763, Aug. 1983.

[5]Siclari, M. J., "Supersonic Nonlinear Potential Flow Analysis – Interim Report," NASA CR-172456, Aug. 1984.

[6]Pittman, J. L., Miller, D. S., and Mason, W. H., "Supersonic, Nonlinear, Attached Flow Wing Design for High Lift With Experimental Validation," NASA TP-2336, Aug. 1984.

[7]Siclari, M. J., "Computation of Nonlinear Supersonic Potential Flow Over Three-Dimensional Surfaces," *Journal of Aircraft,* Vol. 20, May 1983, pp. 462–468.

[8]Siclari, J. J. and Pittman, J. L., "Application of NCOREL to Aircraft Configurations," AIAA Paper 86-1830, June 1986.

[9]Grossman, B. and Siclari, M. J., "The Non-Linear Supersonic Potential Flow Over Delta Wings," AIAA Paper 80-0269, Jan. 1980.

[10]Allen, J. M. and Pittman, J. L., "Analysis of Surface Pressure Distributions on Two Elliptic Missile Bodies," *Journal of Spacecraft and Rockets,* Vol. 21, Nov.–Dec. 1984, pp. 528–533.

[11]Siclari, M. J., "Application of NCOREL to Conical Multi-Finned and Multi-Faceted Configurations," AIAA Paper 86-0441, Jan. 1986.

[12]Pittman, J. L., "Supersonic Airfoil Optimization," AIAA Paper 86-1818, 1986.

[13]Pittman, J. L., Miller, D. S., and Siclari, M. J., "Supersonic Full-Potential Method Applied to Missile Bodies," *Progress in Astronautics and Aeronautics—Tactical Missile Aerodynamics,* edited by M. J. Hemsch and J. N. Nielsen Vol. 104, AIAA, New York, 1986, pp. 632–668.

[14]Smith, J. H. B., Beasley, J. A., Short, D., and Walkden, F., "The Calculation of the Warp to Produce a Given Load and the Pressure Due to a Given Thickness on Thin Slender Wings in Supersonic Flow," ARC R&M 3471, 1967.

[15]Kulfan, R. M. and Sigalla, A., "Real Flow Limitations in Supersonic Airplane Design," AIAA Paper 78-147, Jan. 1978.

[16]Stanewsky, E. and Little, B. H., Jr., "Studies of Separation and Reattachment in Transonic Flow," AIAA Paper 70-541, May 1970.